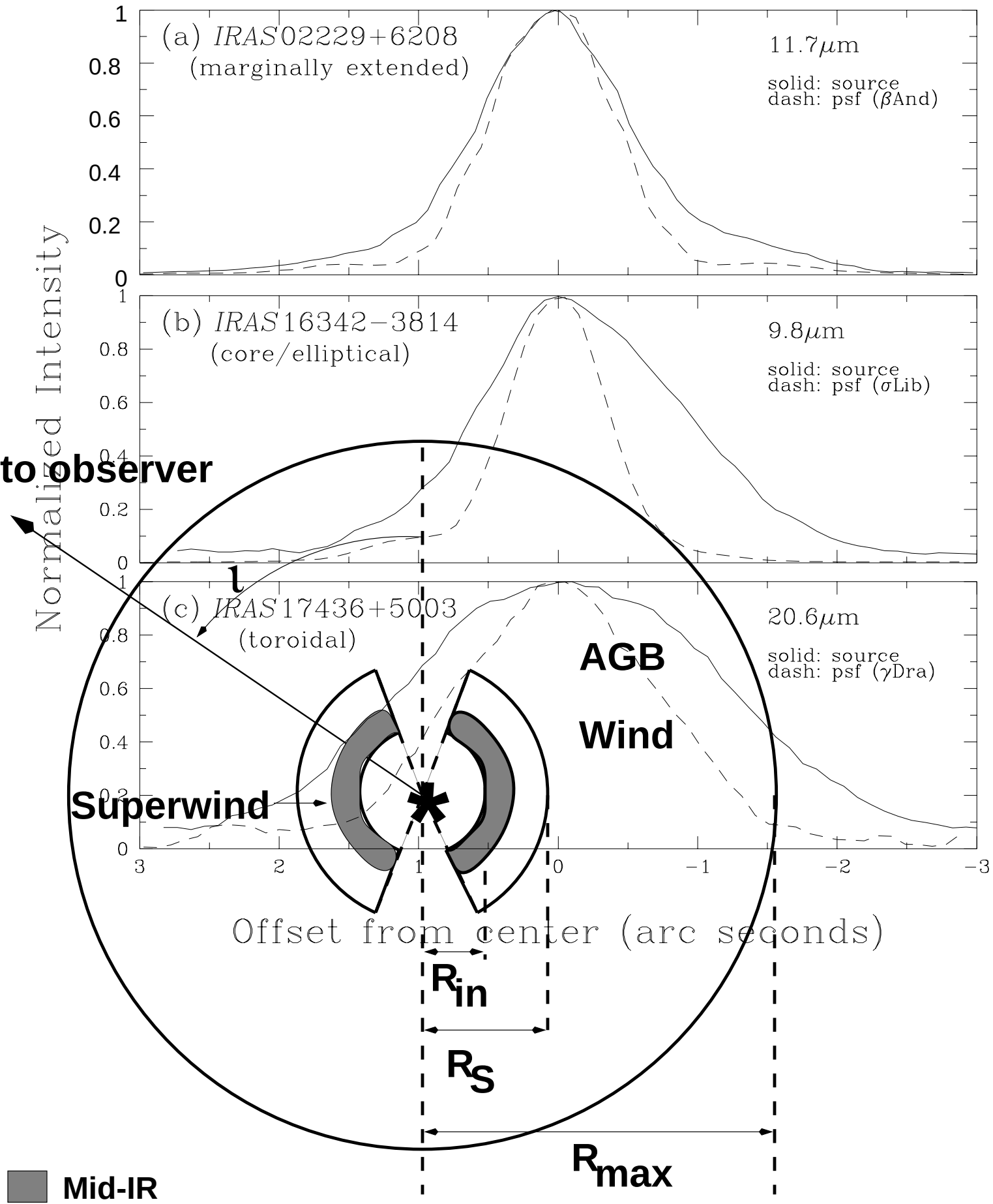
(a) IRAS02229+6208
(marginally extended)
11.7μm
solid: source
dash: psf (βAnd)
(b) IRAS16342−3814
(core/elliptical)
9.8μm
solid: source
dash: psf (σLib)
(c) IRAS17436+5003
(toroidal)
20.6μm
solid: source
dash: psf (γDra)
Normalized Intensity
Offset from center (arc seconds)
to observer
ι
AGB
Wind
Superwind
Rin
RS
Rmax
Mid-IR

arXiv:astro-ph/9812279v1 15 Dec 1998

A Mid-Infrared Imaging Survey of Proto-Planetary Nebula Candidates

Margaret Meixner and Toshiya Ueta

Dept. of Astronomy, MC-221, University of Illinois, Urbana, IL 61801,

meixner@astro.uiuc.edu, ueta@astro.uiuc.edu

Aditya Dayal

IPAC/JPL, Caltech, MS 100-22, 770 South Wilson Ave. Pasadena, CA 91125,

adayal@ipac.caltech.edu

Joseph L. Hora and Giovanni Fazio

Harvard-Smithsonian Center for Astrophysics, MS 65, 60 Garden St., Cambridge, MA 02138, jhora@cfa.harvard.edu, gfazio@cfa.harvard.edu

Bruce J. Hrivnak

Dept. of Physics & Astronomy, Valparaiso University, Valparaiso, IN 46383

bhrivnak@exodus.valpo.edu

Christopher J. Skinner

deceased

William F. Hoffmann

Univ. of Arizona, Steward Obs., Tucson, Az 85721, whoffmann@as.arizona.edu

Lynne K. Deutsch

Boston Univ., Dept. of Astronomy/CAS 519, 725 Commonwealth Avenue, Boston, MA, 02215, deutschl@bu.edu

Received _____; accepted to ApJS May 1999 issue

ABSTRACT

We present the data from a mid-infrared imaging survey of 66 proto-planetary nebula candidates using two mid-IR cameras (MIRAC2 and Berkcam) at the NASA Infrared Telescope Facility and the United Kingdom Infrared Telescope. The goal of this survey is to determine the size, flux, and morphology of the mid-IR emission regions, which sample the inner regions of the circumstellar dust shells of proto-planetary nebulae. We imaged these proto-planetary nebulae with narrow-band filters ($\Delta\lambda/\lambda \sim 10\%$) at wavelengths of notable dust features. With our typical angular resolution of $1''$, we resolve 17 sources, find 48 objects unresolved, and do not detect 1 source. For several sources, we checked optical and infrared associations and positions of the sources. In table format, we list the size and flux measurements for all the detected objects and show figures of all the resolved sources. Images for all the detected objects are available on line in FITS format from the Astronomy Digital Image Library at the National Center for Supercomputing Application. The proto-planetary nebula candidate sample includes, in addition to the predominant proto-planetary nebulae, extreme asymptotic giant branch stars, young planetary nebulae, a supergiant, and a luminous blue variable. We find that dust shells which are cooler ($T \sim 150$ K) and brighter in the infrared are more easily resolved. Eleven of the seventeen resolved sources are extended and fall into one of two types of mid-IR morphological classes: core/elliptical or toroidal. Core/elliptical structures show unresolved cores with lower surface brightness elliptical nebulae. Toroidal structures show limb-brightened peaks suggesting equatorial density enhancements. We argue that core/ellipticals have denser dust shells than toroidals.

Subject headings: stars: AGB and post-AGB — stars: mass loss — circumstellar matter — infrared: continuum

1. Introduction

Proto-Planetary Nebulae (PPNe) are objects in transition between the asymptotic giant branch (AGB) and planetary nebula (PN) phases of stellar evolution for intermediate mass stars ($\sim 0.8{-}8.0$ $M_{\odot}$). Like PNe, PPNe are composed of central stars and detached circumstellar envelopes of gas and dust; however, unlike PNe, their central stars are too cool ($T_{eff} < 10^4$ K) to photoionize the envelopes (Kwok (1993)). Hence, we cannot observe the structure of PPNe circumstellar envelopes using high spatial resolution imaging of ionized gas lines or free-free radio continuum that are successfully used for PNe. Instead, techniques which are sensitive to dust (e.g. thermal emission at infrared wavelengths or scattering at visible wavelengths) or neutral gas (e.g. CO or OH mapping in radio) must be used.

In this paper, we present results of a mid-infrared (mid-IR; $8{-}25$ μm) imaging survey of 66 PPN candidates. These images are sensitive to the thermal dust emission arising from the inner-most regions of the PPNe circumstellar dust shells. Figure 1 shows our working model for the circumstellar dust shell created by the AGB and superwind mass loss episodes (cf. Meixner et al. (1997)). If the mass loss velocity is relatively constant over time, then an increasing radial distance in the dust shell corresponds to a time further in the past. The outer regions of the dust shell consist of material that was ejected further in the past than material in the inner regions. The inner radius of the dust shell marks the point in time when the mass loss ended. The "superwind" region marks the location of material ejected during an intense and perhaps axially symmetric mass loss phase that ends a star's life on the AGB. The central star heats the dust shell directly and, hence, the temperature of the dust decreases with increasing radial distance from the central star. Judging from the spectral energy distributions of many PPNe, the temperature of the dust at the inner radius is about a few 100 K (Volk & Kwok (1989)). Warm dust (i.e. at a few 100 K) emits primarily in the mid-IR. Hence, the mid-IR emission arises from the inner radius out into

the superwind region to a radial distance where the dust temperature drops below a 100 K (shaded region of Fig. 1; Meixner et al. (1997)). The purpose of this survey is to determine the size and morphology of the mid-IR emitting regions. The size of this region gives us direct information on the inner radius of the dust shell and the extent of the warm dust. The morphology of this region shows the geometry of the superwind phase.

We selected our sample of 66 PPN candidates from many articles in the literature and our personal knowledge of the sources. To provide a context for our discussions below, we have created Table 1, which lists some pertinent characteristics of each these PPN candidates from the literature. Included in Table 1 is the source's *IRAS* ID, its chemistry (C = carbon-rich/C-rich, O = oxygen-rich/O-rich, C/O = both C-rich and O-rich), the spectral type of the central star, the visual magnitude of this central star, the *IRAS* fluxes in Jy, the reference for a mid-IR spectrum, a distance estimate, and references for the listed information. When information is not listed, it means that it could not be found. A brief look at Table 1 shows the breadth of the sample of PPNe that we imaged in this survey: an almost even mix of C- and O-rich sources, a spread of spectral types from M to O, and a range of infrared brightnesses ($F_{25} = 2.4 - 2314$ Jy) and visual magnitudes (24−5.5). In Roman numeral footnotes, we note 14 of the sources which are not strictly PPNe, but very young planetary nebulae (Young PN), extreme AGB stars[1], or other. For brevity, we refer to this entire sample as PPNe or PPN candidates hereafter.

The remainder of this paper covers the observations (section 2), the results (section 3), a brief discussion of the results (section 4), and the conclusions (section 5). However, the bulk of the information can be found in Tables 1, 2, & 3 and the figures.

[1]An extreme AGB star is a heavily dust enshrouded star in the process of its final mass loss episode. Extreme AGB stars are at the so-called tip of the AGB.

2. Observations and Data Reduction

Observations of the PPN candidates were obtained using two different mid-IR cameras, MIRAC2 and Berkcam, between 1991 and 1995. The specific observing parameters for each PPNe are listed in Table 2. In particular, the positions recorded in this table were the positions at which we found the sources and are accurate within a few arcseconds. The angular resolution, which can be assessed for individual images by looking at the point spread function (PSF) size in Table 3, is typically about 1″. Diffraction effects dominate the angular resolution for many of the images. For a 3 m telescope, the diffraction-limited angular resolution is $\sim 0.''8$ at 10 μm. Below we describe the general observation strategy used with the MIRAC2 and the Berkcam mid-IR cameras.

2.1. MIRAC2

We obtained images of 52 PPN candidates using MIRAC2, the University of Arizona/SAO mid-IR camera (Hoffmann et al. (1998)), at the 3.0 m NASA Infrared Telescope Facility (IRTF) and at the 3.8 m United Kingdom Infrared Telescope (UKIRT). The dates of the observations span three observing runs: (1) 1995 June 3−7 at IRTF, (2) 1995 November 6, 7, 10 at IRTF, and (3) 1995 November 22−24, 28 at UKIRT. The weather was clear and calm for the entire 1995 June run, was mostly clear for the 1995 Nov IRTF run and was mostly cloudy for the 1995 Nov UKIRT run. The array is a Boeing HF-16 arsenic-doped silicon blocked-impurity-band hybrid array and has a 128×128 pixel format. The pixel scale, which can be changed with a zoom magnification, was set to $0.''39$ for the 1995 June run, to $0.''34$ for the 1995 Nov IRTF run, and $0.''28$ for the 1995 Nov UKIRT run. These pixel scales ensure a Nyquist sampling of the diffraction-limited PSF at both telescopes. The fields of view were $50'' \times 50''$, $44'' \times 44''$, and $36'' \times 36''$, respectively. Wavelengths of observations are selected using interference filters (bandwidths listed in

Table 2) or circular variable filters (labelled as CVF with corresponding bandwidth in Table 2). The strategy was to image these PPNe at wavelengths of known dust features in the mid-IR and at wavelengths of the dust continuum. Mid-IR spectra, when available, were used for guidance in selecting wavelengths. We used the standard method of chopping and nodding to sample the sky background emission in the mid-IR. The secondary was chopped by 20″ south at a $\sim$ 3 Hz rate and the telescope was nodded by 20″ west at a $\sim$ 0.07 Hz rate. For *IRAS* 18184-1623, which is more extended, the chop and nod throws were increased to 40″. The CGS3 standard stars (cf. Cohen & Davies (1995)) were used for flux and PSF calibration. We observed standard stars before and after the sources to check for variations in the PSF. For high declination sources at the IRTF, we used K giants near the source (within a few degrees) as PSF standards because there are no flux standards at these high declinations. This additional PSF check is particularly necessary because the IRTF has an astigmatism which affects the PSF, especially at high declinations.

For each observed wavelength of a source, we obtained $\sim$10 sets of nod-chop cycles where each nod-chop cycle consists of 2 nod sets (1 on; 1 off) and each nod set contains 2 chopped frames (1 on; 1 off) for a total of 4 frames for a nod-chop cycle. Using our own software, we first subtracted the chop-off from the chop-on frames and then subtracted the nod-off from the nod-on frames; and thereby, obtained sky-subtracted, co-added images in which the source appears in all four beams (two positive and two negative). A gain matrix to flat field the images was derived from images of the dome (high intensity, uniform background) and the sky (low intensity, uniform background) and applied to the sky-subtracted, co-added images. A mask file to block out the effects of bad pixels and field vignetting was created and applied to these flat-fielded images. The images were further processed using IRAF[2] routines. In order to cross correlate the multiple sky-subtracted,

[2]Image Reduction and Analysis Facility is distributed by the National Optical Astronomy

co-added images on a sub pixel scale, we first magnified the images by a factor of four, using a linear interpolation and conserving the flux. The resulting images had pixel sizes 1/4 of their original size: 0.″098/pixel for the 1995 June run, 0.″085/pixel for the 1995 Nov IRTF run, and 0.″070/pixel for the 1995 Nov UKIRT run. The multiple sky-subtracted, co-added images of each source were cross-correlated, realigned, summed, and dissected into four individual images of the source. These four images were cross-correlated, realigned and summed to produce the final image. The same observing and reduction procedures were used for the standard stars and the sources; thus any effect of these procedures on the resultant images of the sources and standards should be the same. Typical integration times on source are 70 seconds, resulting in typical one sigma, rms noise of 1.1 mJy arcsecond^{-2}.

2.2. Berkcam

Observations and data reduction with Berkcam followed a similar strategy as observations with MIRAC2 and we describe the main differences here. We observed 14 PPN candidates using Berkcam, which had a 10×64 Hughes Aircraft, Si:As, RIBIT (Reversed Illuminated Blocked Impurity Transmission) array (Arens et al. (1987); Keto et al. (1992)). The observations were made in 1992 June and 1992 December at UKIRT and in 1991 May at IRTF. The weather on all nights of observations was clear. The pixel scale was 0.″39. The resulting small field of view (4″×25″) of the array required us to mosaic images of all sources and standard stars with 3−5 array panels in order to cover the entire image of the object. Chopping the secondary with a 10″−40″ throw at a rate of 6.5 Hz and nodding the telescope with a 20″−40″ throw every 5−15 seconds was performed to measure the sky

---

Observatories, which is operated by the Association of Universities for Research in Astronomy, Inc., under cooperative agreement with the National Science Foundation.

background (cf. Ball et al. (1992)). The standard stars were observed before and after each of the sources. The differences in airmasses between the standard stars and sources were small (< 0.2).

We used IRAF for the initial stages of data reduction. We first obtained sky-subtracted, co-added images, similar to those we obtained for the MIRAC data, except that a partial source appears once, sometimes twice on the final image depending on the size of the chop and nod throws. We derived flat fields directly from sky frames from which we subtract dark frames and applied them to the sky-subtracted, co-added images. In order to stitch together the 3-5 panel mosaics of images on a subpixel scale, we first magnified by a factor of four, resulting in a pixel size of $0.''098$/pixel. The sky-subtracted, flat-fielded, magnified mosaic panels were then stitched together using an automatic mosaicing program, which we developed and that determines the correct relative offsets for the panels using a minimum least-squares error in the flux differences as a criterion. Typical one sigma rms noise of the images is 46 mJy arcsec^{-2}.

2.3. Flux calibration

We flux-calibrated our source by comparing the source counts (analog to digital units; ADUs) with the standard star counts. Extinction corrections were negligible and not applied because the airmass differences between the standard star and source were kept to less than 0.2. The conversion from ADU to Janskys is done by the following equation;

$$\mathrm{F}_{\nu}^{\mathrm{src}}(\mathrm{Jy}) = \frac{\mathrm{F}_{\nu}^{\mathrm{src}}(\mathrm{ADU})}{\mathrm{F}_{\nu}^{\mathrm{std}}(\mathrm{ADU})} \times \mathrm{F}_{\nu}^{\mathrm{std}}(\mathrm{Jy}), \tag{1}$$

where F_{ν}^{src} (F_{ν}^{std}) is the source (standard) flux density at the observed wavelength ($\lambda = \frac{\nu}{\mathrm{c}}$). The flux densities for the standards are from the CGS3 Standard Table and are specified for wavelengths of 8.65, 10, 11.5 and 19.3 μm (cf. Cohen & Davies (1995)). For many of the

wavelengths, we needed to interpolate values from the table and we assumed a power-law relation between flux and wavelength:

$$F_{\nu}^{\rm std}({\rm Jy}) = F_{\nu_0}^{\rm std}({\rm Jy}) \left(\frac{\lambda}{\lambda_0}\right)^{\beta}, \quad (2)$$

where λ (λ_0) is observed (tabulated) wavelength and β is the power-law coefficient derived from our interpolation between two values of the CGS3 Standard Table. The values for β average -1.9±0.1 for all the stars, in the wavelength ranges 10-11.5 and 11.5-19.3 μm, which is close to -2, the value expected for the Raleigh-Jeans approximation in this wavelength range. The value for β in the wavelength range, 8.65-10 μm for those stars with an SiO absorption band is more shallow, an average of -1.6±0.2, because the SiO absorption band at 8 μm causes an apparent rise in flux between 8 and 10 μm relative to the expected -2 fall off (Cohen & Davies (1995)). Absolute flux calibration errors are at least 10%. Photometry of the 1995 Nov UKIRT data was not reliable due to poor weather conditions, and is not reported in Table 3.

3. Results

Of the 66 PPN candidates, 17 (26%) are resolved, 48 are unresolved and 1 is undetected. In this section, we present the sizes and fluxes of the mid-IR emission region of the 65 detected PPN candidates and discuss the images of two unresolved sources and all seventeen resolved sources. In section 3.1, we describe our method for measuring the sizes and fluxes listed in Table 3. In section 3.2, we talk about optical associations for the infrared components of some PPN candidates and the undetected source. In section 3.3, we describe how we determined whether or not our mid-IR images resolve the sources. The cross cuts of three resolved sources and their PSFs (Figure 2) illustrate three categories: marginally resolved, core/elliptical and toroidal. In sections 3.4 and 3.5, we discuss, respectively, the marginally resolved sources and extended sources, of which core/ellipticals and toroidals

are two distinct subcategories.

3.1. Measurements

In Table 3, we list the measured properties of the sources for each observed wavelength: flux density, size and ellipticity of source, and, for comparison, size and ellipticity of the PSF. Most objects have at least two PSFs (before and after) for comparison. We obtain these measurements by fitting isophotal ellipses to the infrared emission. Total flux density is summed within the 3σ isophote. From the isophote with 50% of the peak intensity, we measure the size (Size), ellipticity (EL), and position angle (PA). Size is the major axis length in arcseconds. EL is defined as EL $= 1 - b/a$, where a (b) is the major (minor) axis length. PA is measured in degrees from north toward east (counter-clockwise in the sky).

3.2. Optical Associations and Non-detections

A number of these PPNe have supposed optical associations established by either cross correlating optical star catalogs and the *IRAS* catalog or by looking for optical counterparts on the all sky survey within the *IRAS* error ellipse. During this mid-IR imaging survey, we found that some of these optical associations are correct and others are not. We determined the validity of an association by finding the optical counterpart in the telescope optical guide camera, and checking the position of the corresponding mid-IR image on the array. The alignment between the optical guide camera and the mid-IR camera was established by imaging standard stars which are bright at optical and mid-IR wavelengths. We confirmed the optical associations for *IRAS* 00470+6429, *IRAS* 04386+5722, and *IRAS* 19386+0155. *IRAS* 22480+6002 had two possible optical associations, both bright stars separated by $10''$ east-west, which fall within the position error ellipse. We found that *IRAS* 22480+6002

is associated with the brighter star that lies west in the pair. We also found that HD 235718 (SAO 34043) is not associated with *IRAS* 22036+5306, and that there is no infrared counterpart to HD 235718. We do not detect mid-IR emission from HD 20041 which Oudmaijer et al. (1992) claim is associated with *IRAS* 03119+5657.

3.3. Criteria for Resolving Sources

We determine if a source is extended, marginally resolved or unresolved by systematically comparing the source size with its PSF size in two ways: a visual comparison of the source and PSF images and cross cuts (e.g. Fig.2), and a quantitative comparison of the source and PSF sizes listed in Table 3. For the quantitative comparison, we calculate a source-to-PSF size ratio for each wavelength, and then obtain an average ratio for all observed wavelengths. For reference, we also calculate a [larger PSF]-to-[smaller PSF] ratio from the before and after source observations of PSFs and find an average ratio of 1.08±0.1 for all the PSFs and an average ratio of 1.06±0.07 if we exclude UKIRT data. We claim that a source is extended if this averaged source-to-PSF size ratio is larger than 1.3 and unresolved if the averaged source-to-PSF size ratio is smaller than 1.1. Sources that have averaged source-to-PSF size ratios between 1.1 and 1.3 are considered marginally resolved, depending on the quality and quantity of the data. For example, several sources which were observed during the 1995 Nov UKIRT run fall into this 1.1 to 1.3 range; however, we do not think any of them are resolved because of the variable seeing during that run. The IRTF images were taken with much better seeing but some of them are affected by astigmatism (see below). Sources with ratios between 1.1 and 1.3 at more than one wavelength (e.g. *IRAS* 02229+6208) are considered marginally resolved, while others in this range, for which we have data at only one wavelength (e.g. *IRAS* 17534+2603), are unresolved. *IRAS* 06176−1036 (Red Rectangle) is an exception to the above quantitative

criteria. Visual comparison of *IRAS* 06176−1036 and its PSF shows that it is most certainly extended at the 20% contour level, but quantitative comparison suggests that it is unresolved because it is unresolved at the 50% contour level used in our quantitative criteria.

Using the above criteria, we determine that a total of 17 sources are resolved; 11 are clearly extended and 6 are marginally resolved. We summarize information about the resolved sources in Table 4A: *IRAS* ID, mid-IR size, mid-IR morphological class, chemistry, type of object, and optical morphology. Looking at Table 1, where the general observed properties of these PPNe candidates are listed, we ask the question: Are there any physical characteristics which determine whether or not a source is resolvable? Distance of the source, the luminosity of the central star and the inner radius of the dust shell are three important factors because if a source is closer it is more easily resolved, if it is more luminous the size of the warm dust emission region is larger, and if the inner radius of the dust shell is larger it is more easily resolved. In Table 1, we list distance (D) estimates for some sources, but these estimates are reliable only to a factor of a few and, hence, the luminosities (L) for the sources are also not well known. However, if we compare the Table 1 *IRAS* fluxes of the sources, which are proportional to LD^{-2}, we find that sources which are resolved tend to have higher fluxes, and hence are closer or more luminous or more luminous and closer than the unresolved sources. Inner radii of the dust shells are not known; in fact these mid-IR images are the best sources for this information. However, the temperature of the dust, as determined from the infrared spectral energy distribution (SED), can yield an estimate on the inner radius. Cooler ($\sim$ 150K) dust shells, where the SED peaks at 25μm, have larger inner radii than warmer ($>$ 300K) dust shells, where the SED peaks at 12μm or shorter wavelengths, because the dust is cooler when it is further from the central star which heats it (Volk & Kwok (1989)). All of the sources that are resolved, except *IRAS* 06176-1306, are significantly brighter ($\times$2-10) at 25μm compared to

12μm, while many of the unresolved sources are brighter at 12μm compared to 25μm. Thus we conclude that sources which have brighter and cooler infrared fluxes are more easily resolved. We add one speculative footnote to this discussion. The three faintest resolved sources, *IRAS* 20000+3239, *IRAS* 22223+4327 and *IRAS* 23304+6147, all have SEDs which peak at 25μm but are not particularly bright compared to other sources in Table 1. All three of these sources are C-rich and two have dust features attributed to polycyclic aromatic hydrocarbons (PAH) in their mid-IR spectra (the third has no published mid-IR spectrum; cf. Table 1). We suggest that the PAH dust emission in these sources tends to be more extended than one would expect from dust grains in thermal equilibrium; thereby making it easier to resolve these sources.

3.4. Unresolved and Marginally Resolved Sources

The images of two unresolved sources and all of the seventeen resolved sources are shown in Figure 3 and comments about each source appear in appendix A. The MIRAC2 images of *IRAS* 07399−1435 and all of the sources imaged with Berkcam have been presented in a preliminary form by Dayal (1997) and Meixner (1993a), respectively.

The two unresolved sources, *IRAS* 16559−2957 and *IRAS* 22480+6002, show two extremes in the quality of PSFs. The image of *IRAS* 16559−2957 is a very good example of an unresolved source: the source looks exactly like the PSFs. The PSFs for *IRAS* 16559−2957 are also nicely round. The images of *IRAS* 22480+6002 and its PSFs are presented to show how IRTF astigmatism affects the shape of the images, particularly at high declinations. *IRAS* 22480+6002 has a cross appearance: a main NE-SW elongation with some perpendicularly extended structure. The standard star β Peg, which is at a significantly lower declination, has a very round appearance, and thus one might think that *IRAS* 22480+6002 is extended. However, the image of a K star nearby *IRAS* 22480+6002

($< 1^\circ$ separation) has an appearance similar to the image of *IRAS* 22480+6002. Thus, this elongation is an artifact, caused by a known astigmatism problem with the IRTF. Hence, we consider such elongations and cross structures, particularly for high declination sources, also to be artifacts. *IRAS* 23304+6147, discussed below, is an example of a marginally extended source affected by this astigmatism.

The six marginally-resolved sources are: *IRAS* 02229+6208, *IRAS* 17441−2411, *IRAS* 18184−1302, *IRAS* 18276−1431, *IRAS* 20000+3239, and *IRAS* 23304+6147 (Figure 3). The cross-cut of *IRAS* 02229+6208 displays a comparison of a marginally resolved source with its PSF (Fig. 2). Three of these sources, *IRAS* 02229+6208, *IRAS* 20000+3239, and *IRAS* 23304+6147, are cool (T ∼150 K), C-rich PPNe with features at 21 μm. Two sources, *IRAS* 17441−2411 and *IRAS* 18276−1431, are cool, O-rich PPNe. *IRAS* 18276−1431 is marginally extended at 9.8 μm but unresolved at 12.5 μm. The remaining source, *IRAS* 18184−1302, is probably a pre-main sequence star which was included as a PPN candidate because of its cool *IRAS* colors.

3.5. Extended Sources: Core/Elliptical vs. Toroidal

Eleven sources are extended (source-to-PSF ratio > 1.3), ten of which appear to have an axial symmetry. The axial symmetry observed in the extended images seems to fall into two distinct morphological classes: (1) core/elliptical and (2) toroidal (Table 4A). The core/ellipticals have unresolved, very bright cores that are surrounded by a lower surface brightness elliptical nebula. The toroidals have some evidence for two peaks that are interpreted as limb-brightened peaks of an equatorial density enhancement. Cross cuts through the images of the core/ellipticals and toroidals help to illustrate these differences (Fig. 2). Core/ellipticals are strongly peaked with a broad pedestal, while toroidals have a plateau-like appearance when the two peaks are not quite resolved.

3.5.1. Core/ellipticals

Eight of the sources are core/ellipticals: *IRAS* 06176−1036 (Red Rectangle), *IRAS* 07399−1435 (OH231.8+4.2), *IRAS* 16342−3814, *IRAS* 17028−1004 (M2−9), *IRAS* 17150−3224, *IRAS* 17347−3139, *IRAS* 19244+1115 (IRC+10420) and *IRAS* 19374+2359 (Figure 3). All but one, *IRAS* 06176−1036, are O-rich. *IRAS* 16342−3814 is a particularly striking core/elliptical source. The elliptical nebulae in *IRAS* 16342−3814 extends NE-SW with the same PA for all wavelengths. The cross-cut through the major axis of this nebula reveals the contrast between the unresolved core and the lower surface brightness nebula (Fig. 2). The apparent increase in this elliptical nebula's size from the 12.5 μm image to the 20.6 μm image is due largely to the telescope's diffraction effects which limit the angular resolution of the images. For diffraction limited images of point sources, we expect the image size to scale proportionally with the wavelength (λ); specifically, for images at 12.5 μm and 20.6 μm we expect an increase of 20.6/12.5 or 1.65. The ratio of the 20.6 μm size to the 12.5 μm size of the standard star PSFs observed with *IRAS* 16342−3814 is $\sim$1.6. The ratio of sizes for *IRAS* 16342−3814 is a slightly smaller value of 1.3 which we expect because *IRAS* 16342−3814 is not a point source and is better resolved at 12.5 μm than at 20.6 μm.

In five of the O-rich core/ellipticals, the 9.8 μm image appears larger than the images at neighboring wavelengths (8.8, 11.7, or 12.5 μm). The source sizes for *IRAS* 07399−1435, *IRAS* 16342−3814 and *IRAS* 17347−3139 are notably larger at 9.8 μm than at neighboring wavelengths. For *IRAS* 17150−3224 and *IRAS* 19374+2359, we find that the source is marginally larger at 9.8 μm than at 12.5 μm. In addition, *IRAS* 18276−1431 (OH 17.7−2.0), which is also an O-rich source, is marginally resolved at 9.8 μm but unresolved at 12.5 μm. All six of these O-rich sources have a silicate absorption feature at 9.8 μm (see Table 1 for spectral reference and Table 3 for flux values). Thus, the fact that the intensity

at 9.8 μm is more extended that the intensity at neighboring wavelengths appears to be correlated with the presence of a 9.8 μm silicate absorption feature observed in these sources.

IRAS 06176−1036 (Red Rectangle), which has both C-rich and O-rich dust components (cf. Table 1), has an almost reversed appearance compared to these O-rich sources. It is smaller at 10 μm than at its neighboring wavelengths, 8.2 and 11.3 μm as has also been found in previous studies (Hora et al. (1996); Bregman et al. (1993);Sloan, Grasdalen & Levan (1993)). The PAH emission features at 8.2 and 11.3 μm (cf. Table 1) appear to be brighter in the low level elliptical nebula than the 10μm continuum dust emission which samples the non-PAH dust grains and may be sampling the O-rich dust component (Waters et al. 1998).

3.5.2. Toroidals

We classify three objects as toroidals: *IRAS* 17436+5003, *IRAS* 18184−1623 and *IRAS* 22223+4327 (Figure 3). The toroidal sources show evidence of a central torus of dust. *IRAS* 17436+5003 (HD 161796) has resolved inner contours that are elongated east-west this is the same direction that Skinner et al. (1994) resolved two peaks of a toroidal structure at 12.5 μm in this object. The cross cut of *IRAS* 17436+5003 (Fig. 2) shows a plateau-like, flattened top which is expected when two limb brightened peaks are just beyond the resolution limit. *IRAS* 22223+4327 is similar in morphology to *IRAS* 17436+5003 and has a plateau-like cross-cut similar to that of *IRAS* 17436+5003. Although we do not have other evidence that this inner region will resolve into two limb-brightened peaks, similarities between *IRAS* 22223+4327 and the other toroidal sources found in the literature (discussed below) strongly suggest that it is toroidal.

IRAS 18184−1623 shows a remarkable dust shell which is clearly detached from the central star. Both 8.8 and 12.5μm images show the central star surrounded by a partially complete ring structure that has two peaks, almost symmetric around the star. We interpret these two peaks as limb-brightened peaks of an equatorial density enhancement, i.e. a torus of dust; hence we classify this object as a toroidal source. If one were to convolve *IRAS* 18184−1623 with a PSF that had a FWHM equal to the separation of its two peaks, one would find a source structure similar to that in *IRAS* 17436+5003 and *IRAS* 22223+4327. The 20.6 μm image also shows this dust shell structure; however the central star is too faint to appear at the center. Comparing all three wavelengths in *IRAS* 18184−1623, we find that the parts of the dust shell perpendicular to the torus change. At 8.8 μm, the dust shell is filled in at the southern edge and partially filled at the northern edge. As the wavelength increases, we find this southern edge disappearing while the northern edge gains more prominence, particularly at 20 μm. This change in morphology could be due to different temperatures of the dust in these regions, i.e. the southern edge is warmer than the northern edge, or, there could be differences in grain types. Mid-IR spectroscopy of this nebula would help to answer these questions. *IRAS* 18184−1623 has been classified as a luminous blue variable (LBV), and the toroidal structure that we observe here has been observed on comparable size scales at other wavelengths, e.g. Hα (Hutsemekers et al. (1994); Nota et al. (1996)), near-IR and mid-IR (Robberto & Herbst (1998)).

4. Discussion

Mid-IR images of PPNe show us the size and morphology of the inner regions of the dust shells in these sources. If we enlarge the sample to include other published mid-IR imaging studies, we can add eight additional sources, seven of which are resolved (see Table

4B). Of the 73 PPN candidates for which there exist mid-IR images, only 24 (33%) are resolved. Interestingly, two of the unresolved sources, *IRAS* 10158−2844 (HR 4049) and *IRAS* 15465+2818 (R CrB), have extremely large and cool (T$\sim$ 30 K) dust shells ejected by an ancient mass loss episode (Gillett et al. (1986), Waters et al. (1989)); the mid-IR images do not show these large dust shells, but rather reveal very recently ejected, compact dust shells. Of the 24 resolved sources, 7 are marginally resolved (unknown morphology), 10 have core/elliptical extended structure, and 7 have toroidal extended structures. The resolved sources are almost evenly divided between C-rich (13) and O-rich (11) chemistry. The core/elliptical sources seem to be mostly O-rich (7 out of 10) and the toroidal sources seem to be mostly C-rich (5/7). However, with such small numbers (and presumably some selection effects) it is hard to gauge the significance of these trends with chemistry.

There are three pieces of evidence suggesting that core/ellipticals have denser dust shells than toroidals. Firstly, comparison of the optical morphologies between toroidals and core/ellipticals shows significant differences (Table 4A and 4B). In toroidal sources, the central star is very prominent in the optical image and is usually surrounded by nebulosity that is faint in comparison to the star. In contrast, the central star is rarely seen in the core/elliptical sources and almost all of the optical light is reflection from the nebula. The morphologies of the optical reflection nebulae vary among the toroidals, but almost all the core/ellipticals display optical bipolar nebulae. The optical bipolar reflection nebulae found for core/ellipticals extend in the same direction as the mid-IR elliptical nebula; however, the optical bipolar nebulae are larger than the mid-IR elliptical nebulae. The difference in optical morphology between toroidals and core/ellipticals suggests that toroidals are transparent in the optical whereas core/ellipticals are opaque in the optical.

Secondly, the core/ellipticals are typically O-rich and have deep silicate absorption features at 9.8 μm in the mid-IR spectra which indicate that they are optically thick in the

mid–IR. Our images of the core/ellipticals show that the dust shells are compact and that they appear larger at 9.8 μm than at neighboring wavelengths (8 and 12.5 μm). In order to have an optically thick source which is compact, the dust shell must be very dense. The images together with the mid-IR spectra paint a picture of dense "dust photospheres" that have decreasing temperatures with increasing radial distance from the star. At the more optically thick wavelength of 9.8 μm, we have a shallower view into the "dust photosphere" and the dust shell appears both larger and fainter because the dust shell is physically larger and cooler at this larger radial distance from the star. At neighboring wavelengths, where the optical depth is lower, we have a deeper view into the "dust photosphere" and the dust shell appears smaller and brighter because the dust shell is physically smaller and hotter at this smaller radial distance from the star.

Thirdly, radiative transfer models of the star and dust shell systems reveal marked differences in the densities of toroidals and core/ellipticals. Meixner et al. (1997) model *IRAS* 07134+1005, which is a toroidal, C-rich PPN, and find the dust torus to have low optical depth in the mid-IR ($\tau_{9.7\mu m} \sim 0.03$) and to have an inclination angle of $\sim 45^{\circ}$. Thus the fact that we see the central star in *IRAS* 07134+1005 is not simply due to the viewing angle; we see the central star because the dust density for *IRAS* 07134+1005 is low. On the other hand, Skinner et al. (1997) model the Egg Nebula (AFGL 2688), which is a core/elliptical, C-rich PPN, and find the dusty torus to be optically thick not only in the optical, which has always been presumed based on the obscuring dust lane of the bipolar reflection nebula, but also in the mid-IR and longer wavelengths. Both the high optical depth at 10 μm ($\tau_{10\mu m} \sim 2.4$) and the compact size of the dust shell indicate a high density for the inner regions of the Egg Nebula. These model calculations corroborate the empirical evidence, outlined above, that core/ellipticals have very dense cores which make them optically thick at mid-IR wavelengths. The calculations also show that toroidals are quite different in character to core/ellipticals, i.e. the difference is not just a viewing angle effect.

Why do core/ellipticals have higher density dust shells than toroidals? We suggest that core/ellipticals have experienced overall higher mass loss rates compared to toroidals. For example, the Egg Nebula, a core/elliptical, experienced a mass loss rate of $4 \times 10^{-3} M_{\odot}$ yr^{-1} just before it departed from the AGB (Skinner et al. (1997)); whereas *IRAS* 07134+1005, a toroidal, experienced a significantly lower mass loss rate of 6×10^{-5} $M_{\odot}$ yr^{-1} (Meixner et al. (1997)). Interestingly, both the Egg Nebula and *IRAS* 07134+1005 experienced dramatic increases in mass loss rates by factors of ∼40 and 10, respectively, prior to leaving the AGB (Skinner et al. (1997);Meixner et al. (1997)). Hence, both types of sources, core/ellipticals and toroidals, have experienced superwinds. However, the important factor in creating a core/elliptical as opposed to a toroidal source, is that the superwind mass loss rate is very high; so high that it creates a dense, dusty torus which is optically thick at mid-IR wavelengths and which obscures the central star at optical wavelengths. What causes the higher mass loss rates in core/ellipticals is not clear. It may be that core/ellipticals have higher mass progenitor stars which are thought to experience higher mass loss rates at these later stages.

Future avenues of research with these mid-IR images are both theoretical and observational. The mid-IR images, both resolved and unresolved, are useful constraints for modeling the circumstellar dust shells. Meixner et al. (1997) found that unresolved images provided upper limits on the inner radii of the PPNe dust shells and marginally resolved images provide a precise constraint on the inner radii. Extended images reveal not only the inner radii, but also the geometry and density distribution of the dust shells. We plan to model these sources, using additional information, to derive the physical parameters of these dust shells.

Higher angular resolution would greatly increase the number of resolved sources. What currently limits our angular resolution at mid-IR wavelengths is aperture size; i.e. we are

primarily diffraction limited. With the new 8-10 m aperture telescopes in operation and coming into operation in the near future, angular resolution will improve by a factor of two making it worthwhile to reimage all these sources.

5. Conclusions

Of the 66 PPN candidates imaged at mid-IR wavelengths (8−25 μm), 17 were resolved, 48 were unresolved, and 1 was not detected. We present fluxes, sizes and morphologies for the 17 resolved PPN candidates and fluxes, and upper limits on sizes for the 48 unresolved sources. These data will be useful for modeling the circumstellar dust shells of these sources. The 17 resolved sources have brighter and cooler (peaking at 25μm) *IRAS* fluxes than the unresolved sources which suggests that the resolved sources are closer or more luminous and cooler (T $\sim$150 K) than unresolved sources. For the 11 extended sources, two types of morphology are evident: core/elliptical, e.g. *IRAS* 16342−3814, and toroidal, e.g. *IRAS* 18184−1623. We argue that this difference in morphology corresponds to a difference in dust shell density: core/ellipticals have significantly denser dust shells than toroidals. The denser dust shells of core/ellipticals suggests that they originate from stars with higher mass rates than do the toroidals.

Even though we show only a sub portion of the mid-IR images in this paper, we make all the mid-IR images for all the sources and their PSFs available in FITS format on the World Wide Web's NCSA Astronomy Digital Image Library (ADIL, at URL: http://imagelib.ncsa.uiuc.edu/document/98.MM.02).

MIRAC2 has received support from NASA and NSF. W. Hoffmann was visiting astronomer at the Institute for Astronomy, U. of Hawaii during part of this work. Meixner and Ueta were partially supported by the NSF (AST95-21605 and AST97-33697).

Hrivnak was partially supported by the NSF (AST93-15107) and NASA (NAG 5-1223). The Berkcam observations were partially supported by the Institute of Geophysics and Planetary Physics at Lawrence Livermore National Laboratory. This research made use of the SIMBAD database, operated at CDS, Strasbourg, France, for the *IRAS* fluxes, and many of the visual magnitudes and for a literature search of these sources. We thank the helpful staff at the IRTF and UKIRT for their assistance. We are grateful to the Hughes Aircraft Corporation, who supplied the mid-IR array used in Berkcam.

A. Comments on Objects in Figure 3

In this appendix, we make comments about each source shown in Figure 3. The comments are listed in the order that the source appears in Figure 3.

IRAS 16559−2957 is unresolved and shows nice round PSFs.

IRAS 22480+6002 is an unresolved source with a "cross pattern" that is created by the IRTF astigmatism. Only the source and nearby K star are affected by IRTF astigmatism, and therefore, it is difficult to recognize that the lowest contour structure is an artifact of IRTF astigmatism when one compares images of the source and βPeg, which is unaffected by the astigmatism because of its lower declination.

IRAS 02229+6208 is marginally resolved at all five wavelengths.

IRAS 06176−1036 (Red Rectangle) has an unresolved core at all three wavelengths, but is extended at 8.2 μm, and 11.3 μm at the lower contour levels. Extension at 10 μm is also seen at contour levels less than 10%, the lowest contour level shown here.

IRAS 07399−1435 (OH 231.8+4.2) is extended at all five wavelengths, and is more extended at 9.8 μm than at 8.8 or 11.7 μm. The general increase of size with increasing

wavelength is a diffraction effect (see section 3.5.1).

IRAS 16342−3814 is extended at all four wavelengths. Its size increases from 12.5 μm to 20.6 μm as expected from diffraction effects but it is larger at 9.8 μm than 12.5 μm(see section 3.5.1).

IRAS 17028−1004 (M 2−9) is unresolved at 8.1 and 8.5 μm, marginally resolved at 9.7 μm, and extended at 12.6 and 12.8 μm.

IRAS 17150−3224 is extended at all three wavelengths and is slightly more extended at 9.8 μm than 8.1 or 12.5 μm. The 9.8 μm image shows the shape and PA of the elliptical nebula best because the 8.1 and 12.5 μm images are affected by artifacts seen in the PSFs.

IRAS 17347−3139 is extended at both 9.8 and 12.5 μm but unresolved at 20.6 μm. It is bigger at 9.8 μm than at 12.5 μm(see section 3.5.1).

IRAS 17436+5003 (HD 161796) is extended at both wavelengths. The inner elliptical contour extends in the same direction as the two peaks resolved at 12.5 μm by Skinner et al. (1994).

IRAS 17441−2411 is marginally extended at both wavelengths. The apparent ellipticity and PA of its extended nebula is a little suspect because we observe the some ellipticity with the same PA in the PSF.

IRAS 18184−1302 (MWC 922) is marginally extended.

IRAS 18184−1623 (HD 168625) is extended at all three wavelengths. The central star, seen at the center, in the 8.8 and 12.5 μm images (but not the 20.6 μm image) serves as a PSF reference. The two peaks in the dust shell are interpreted as limb-brightened peaks of an equatorial density enhancement. The images have been smoothed by a Gaussian ($\sigma = 3$). The contour levels in this image start at 20% and the interval is 20%.

IRAS 18276−1431 (OH 17.7−2.3) is marginally extended at 9.8 μm and unresolved at 12.5 μm.

IRAS 19244+1115 is extended at both wavelengths and exhibits an elliptical nebula.

IRAS 19374+2359 is larger at 9.8 μm that the marginally extended structures seen at 12.5 and 20.6 μm.

IRAS 20000+3239 is marginally resolved at both 8.1 and 12.5 μm (observed at 12.5 μm on two different date, 1995 June 3 and 6). The core extension seen at 12.5 μm image taken in the June 3 run is suspect since βPeg observed after the source (right) shows similar East-West elongation and since the source image taken in the June 6 run does not show such extension.

IRAS 22223+4327 is extended both at 12.5 and 18.0 μm. On both source images, structures suggested by lowest contours are not very reliable due to low signal-to-noise ratio. North-South elongation of the inner-most core at 12.5 μm is suspect since the PSF (middle frame) shows similar extension.

IRAS 23304+6147 is observed at 12.5 μm on two different dates, 1995 June 5 and 6, and is extended, but is diffraction limited at 20.6 μm. The "cross" pattern seen at 10% level of 12.5 μm source images is certainly not real (IRTF astigmatism).

REFERENCES

Arens, J. F., Jernigan, J. G., Peck, M. C., Dobson, C. A., Kilk, E., Lacy, J., & Gaalema, S., 1987, Appl. Opt., 26, 3846

Ball, R., Arens, J. F., Jernigan, J. G., Keto, E., & Meixner, M. 1992, ApJ, 389,616

Bregman, J.D., Rank, D., Temi, P., Hudgins, D. & Kay, L. 1993, 411, 794

Buss, R. H., Jr. Cohen, M., Tielens, A. G. G. M., Werner, M. W., Bregman, J. D., Witteborn, F. C., Rank, D., & Sandford, S. A. 1990, ApJ, 365, L23

Cohen, M. & Davies J. K. 1995, MNRAS, 276, 715

Cohen et al. 1975, ApJ, 196, 179

Dayal, A. 1997, PhD. Thesis, University of Arizona

Dayal, A., Hoffmann, W.F., Bieging, J.H., Hora, J.L., Deutsch, L.K., & Fazio, G.G. 1998, ApJ, 492, 603

Gillett, F. C. & Soifer, B. T. 1976, ApJ, 207, 780

Gillett, F. C., Backman, D. E., Beichman, C., & Neugebauer, G. 1986, ApJ, 310, 842

Groenewegen, M. A. T., Whitelock, P. A., Smith, C. H., & Kerschbaum, F. 1998, MNRAS, 293, 18

Hawkins, G.W., Skinner, C.J., Meixner, M.M., Jernigan, J.G., Arens, J.F. Keto, E., & Graham, J. 1995, ApJ, 452, 314

Hoffmann, W. F., Hora, J. L., Fazio, G. G., Deutsch, L. K. & Dayal, A. 1998, in Infrared Astronomical Instrumentation, ed. A. M. Fowler, Proc. SPIE 3354, in press

Hora, J. L., Deutsch, L. K., Hoffmann, W. F., & Fazio, G. G. 1996, AJ, 112, 2064

Hrivnak, B. J. 1995, ApJ, 438, 341

Hrivnak, B. J. 1998, unpublished data

Hrivnak, B. J. & Kwok, S. 1991, ApJ, 368, 564

Hrivnak, B. J., Kwok, S., & Boreiko, R. T. 1985, ApJ, 294, 113

Hrivnak, B. J. & Kwok, S. 1998, ApJ, in press

Hrivnak, B. J., Kwok, S.,& Volk, K. M. 1988, ApJ, 331, 832

Hrivnak, B. J., Kwok, S.,& Volk, K. M. 1989, ApJ, 346, 265

Hrivnak, B.J., Langill, P.P., Su, K.Y.L. & Kwok, S. 1999, ApJ, in press

Hu, J. Y., Slijkhuis, S., De Jong, T., & Jiang B. W. 1993a, A&AS, 100, 413

Hu, J. Y., Slijkhuis, S., Nguyen-Q-Rieu & De Jong, T. 1993b, A&A, 273, 185

Humphreys, R.M., Smith, N., Davidson, K., Jones, T.J., Gehrz, R.D., & Mason, C.G. 1997, AJ, 114, 2778

Hu, J. Y., Te Lintel Hekkert, P., Slijkhuis, S., Baas, F., Sahai, R. & Wood, P. R. 1993, A&AS, 103, 301

Hutsemekers, D., van Drom, E., Gosset, E., & Melnick, J. 1994, A&A, 290, 906

Iyengar, K. V. K., & Parthasarathy, M. 1997, A&AS, 121, 45

Justtanont, K., Barlow, M. J., Skinner, C. J., & Tielens, A. G. G. M. 1992, ApJ, 392, L75

Kastner, J.H., Weintraub, D.A., Zuckerman, B., Becklin, E.E., McLean, I., & Gatley, I. 1992, ApJ, 398, 552

Keto, E., Ball, R., Arens, J. F., Jernigan, J. G. & Meixner, M. 1992, International Journal of Infrared and Millimeter Waves, vol. 13, N11:1709

Kwok, S., Hrivnak, B. J., & Geballe, T. R. 1995, ApJ, 454, 493

Kwok, S. 1993, ARA&A, 31, 63

Kwok, S., Hrivnak, B. J., Zhang, C. Y. & Langill, P. L. 1996, ApJ, 472, 287

Kwok, S., Su, K.Y.L., & Hrivnak, B.J., 1998, ApJ, 501, L117

Likkel, L. 1989, ApJ, 344, 350

Loup, C., Forveille, T., Omont, A. & Paul, J. F. 1993, A&AS, 99, 291

Manchado, A., Pottasch, S. R., Garcia-Lario, P., Esteban, C., & Mampaso, A. 1989, A&A, 214, 139

Mauron, N., Le Borgne J.-F., & Picquette, M. 1989, A&A, 218, 213

Meixner, M. 1993, PhD Thesis, UC Berkeley

Meixner, M., et al. 1993, ApJ, 411, 266

Meixner, M., Skinner, C. J., Graham, J. R., Keto, E., Jernigan, J. G., & Arens, J. F. 1997, ApJ, 482, 897

Ney, E.P., Merriall, K.M., Becklin, E.E., Neugebauer, G., & Wynn-Williams, C.G., 1975, ApJ, 198, L129

Nota, A., Pasquali, A., Clampin, M., Pollacco, D., Scuderi, S., & Livio, M. 1996, ApJ, 473, 946

Olnon, F. M., Raimond, E., & IRAS Science Team 1986, A&AS, 65 607

Omont, A., Loup, C., Forveille, T., Te Lintel Hekkert, P., Habing, H.,& Sivagnanam, P. 1993, A&A, 267, 515

Oudmaijer, R.D., van der Veen, W. E. C. J., Waters, L. B. F. M., Trams, N. R., Waelkens, C., & Engelsman, E. 1992, A&AS, 96, 625

Robberto, M. & Herbst, T. M. 1998, ApJ, 498, 400

Silva, A. M., Azcarate, I. N., Poppel, W. G. L. & Likkel, L. 1993, A&A, 275, 510

Skinner, C. J., Meixner, M., Hawkins, G. W., Keto, E., Jernigan, J. G. & Arens, J. F. 1994, ApJ, 423, 135

Skinner, C.J., Meixner, M., Barlow, M.J., Collison, A.J., Justtanont, K., Blanco, P., Piña, R., Ball, J.R., Keto, E., Arens, J.F., & Jernigan, J.G. 1997, A&A, 328, 290

Sloan, G.C., Grasdalen, G.L. & Levan, P.D. 1993, ApJ, 409, 412

Trammell S.R., Goodrich, R.W., & Dinerstein, H.L. 1995, ApJ, 453, 761

Te Lintel Hekkert, P. 1991, A&A, 248, 209

Ueta, T., Meixner, M., & Bobrowsky, M. 1998, in preparation

van der Veen, W. E. C. J., Habing, H. J. & Geballe, T. R. 1989, A&A, 226, 108

Volk, K., & Cohen, M. 1989, AJ, 98, 931

Volk, K., & Cohen, M. 1990, AJ, 100, 485

Volk, K., & Kwok, S. 1989, ApJ, 342, 345

Volk, K., Kwok, S., & Langill, P. P. 1992, ApJ, 391, 285

Volk, K., Kwok, S., & Woodsworth, A. W. 1993, ApJ, 402, 292

Waters, L. B. F. M., Lamers, H. J. G. L. M., Snow, T. P., Mathlener, E., Trams, N. R., van Hoof, P. A. M., Waelkens, C., Seab, C. G., & Stanga, R. 1989, A&A, 211, 208

Waters, L.B.F.M., Waelkens, C., van Winckel, H., Molster, F.J., Tielens, A.G.G.M., van Loon, J. TH., Morris, P.W., Cami, J., Bouwman, J., de Koeter, A., de Jong, T., & de Graaum, Th 1998, Nature, 391, 868

Westbrook, W.E., Becklin, E.E., Merrill, K.M., Neugebauer, G., Schmidt, M. Willner, S.P., & Wynn-Williams, M. J. 1986, ApJ, 304, 401

Young, K., Phillips, T. G. & Knapp, G. R. 1993, ApJS, 86, 517

Zijlstra, A. A., Te Lintel Hekkert, P., Pottasch, S. R., Caswell, J. L., Ratag, M., & Habing, H. J. 1989, A&A, 217, 157

This manuscript was prepared with the AAS LaTeX macros v4.0.

Fig. 1.— A schematic of our working model for proto-planetary nebulae dust shells. The axially symmetric inner regions are created in a superwind mass loss phase. The spherically symmetric outer regions are created in the AGB mass loss phase. The shaded region of this schematic shows where the mid-IR emission arises from the dust shell.

Fig. 2.— Representative examples of cross-cuts of the sources and PSF standards from each morphological class: (a) *IRAS* 02229+6208 (marginally extended, unknown morphology), (b) *IRAS* 16342−3814 (core/elliptical), and (c) *IRAS* 17436+5003 (toroidal). The observed wavelength and identity of corresponding PSF are also indicated in the figure. Solid (dashed) lines show normalized intensity levels of the source (PSF) along the East-West axis. Notice the difference in emission levels around the mid-intensity region ($\sim$ 50% level); (a) *IRAS* 02229+6208 barely shows extended emission, (b) *IRAS* 16342−3814 has a broad pedestal rising to a concentrated core of emission, and (c) *IRAS* 17436+5003 shows a plateau-like emission.

Fig. 3.— Mid-IR images of PPN candidates and their standard star PSFs. Two unresolved PPN candidates appear first followed by the resolved PPN candidates which are shown in order of increasing RA. In each panel, the source appears in the left column, the standard star PSF appears in the middle and right columns. When two PSFs are presented, the first (second) standard star was observed before (after) the source. The object name appears in the top left corner of each image; source names are abbreviated to the RA portion of the *IRAS* name. Each row of the panel corresponds to a different mid-IR wavelength which appears in the bottom right corner of the image as a number in units of μm. The lowest contour levels are 10% and the intervals between contour levels are 20% of the peaks of the images. The peak values appear in the bottom left corner of the image as a number in units of Jy arcsec^{-2}. The coordinate axes show the relative displacement from the peak location in arcseconds. All the images presented, with the exception of *IRAS* 18184-1623,

have the same arcsecond/mm scale on the page for easy comparison. Each row of the figures corresponds to a particular wavelength. Important comments on each of these figures are listed in appendix A.

arXiv:astro-ph/9812279v1 15 Dec 1998

TABLE 1

CHARACTERISTICS OF PROTO-PLANETARY NEBULAE IN MID-IR SURVEY

IRAS ID	C/O[a]	Sp. Type	V	F_{12} [Jy]	F_{25} [Jy]	F_{60} [Jy]	F_{100} [Jy]	Mid-IR Sp.[b]	D[kpc]	Ref.[c]
00210+6221[ii]	C?	...	16.5	48.5	51.9	12.5	...	1	...	A,W,Z
00470+6429	...	...	12.0	4.6	4.9	2.1	10.5	...	...	...
01144+6658[i]	C	...	...	139.9	206.1	64.7	15.9	1	4	A,B
01174+6110	C	...	18.3	4.1	16.9	33.9	30.7	...	...	C,Z
01304+6211	O	...	...	289.0	455.6	194.0	50.2	1	1.5	E
02143+5852	O	F	13.8	5.9	18.1	5.4	...	...	...	...
02152+2822[i]	C	C	...	120.5	112.2	29.6	6.9	1	2.1	E,F
02229+6208	C	G8-K0 Ia	12.1	67	204	31	...	...	...	V
04386+5722	...	M	12.7	18	23	4.4	...	...	...	J
05089+0459	C?	M	14.3	7.4	21.9	11.1	3.8	...	...	J
05113+1347	C	G8Ia	12.4	3.8	15.3	5.5	...	2	...	J,U
05341+0852	C	G2 0-Ia	13.6	4.5	9.9	4.0	...	2	...	V
06176−1036	C/O	B8V	8.8	422	456	173	66	1	0.33	I,AA
06530−0213	C/O	F0Iab	14.0	6.1	27.4	15.1	4.1	...	1.3	G,H,E
07239−3325	...	...	...	1	2.4	...	...	...	...	...
07284−0940[vi]	O	F8Ibe	6.3	124	88.4	26.6	9.5	1	...	F
07331+0021	O	G5Iab	8.8	15.3	68.1	18.5	3.7	...	...	F
07399−1435[i]	O	M6	9.5	19	226.3	548.3	294.0	1,3	1.3	E
07430+1115	C	G5 0-Ia	12.6	7.7	29.9	10.7	2.5	...	...	J,V
08005−2356	C/O	F5e	11.5	18	51.8	29.8	10.4	...	...	J,K
09032−3953	...	...	18.3	20.4	125.9	92.3	28.7	1	...	G
09371+1212	O	K7II	11.0	0.3L	4.6	70.7	28.2	...	...	E,L
10131+3049	C	M	9.4	3319	1219	273.6	86.1	1	0.19	E
10158−2844	C	B9.5Ib-II	5.3	48	9.6	1.8	...	1, 4	3.5	...
11472−0800	...	...	12	11.4	14.2	1.8	...	...	...	...
15465+2818	C	F0-F8pe	5.9	38.9	17.1	3.94	2.0	1,4	1.3	...
16342−3814[i]	O	M	13.7	16.2	199.8	290.2	139.4	1	2.2	M
16559−2957	O	F5Ie	13.2	9.2	32.4	16.4	...	...	...	G,K
17028−1004[ii]	O	B1	14.7	50.5	110.2	123.6	75.8	5,6	1.6	...
17088−4221	O	A0	...	42.7	128.3	106.8	36.9	1	2.4	M
17106−3046	O	...	15.8	4.0	62.4	51.2	17.3	...	...	N,Z
17150−3224	O	G2	14.5	58	322.3	268.3	82.4	1,2	2.42	M,E,O
17245−3951	...	...	15.5	3.4	44.7	38.2	...	1	...	Z
17347−3139[ii]	O	O	...	19	100.3	125.4	249.0	...	...	P
17436+5003	O	F3Ib	7.1	6.12	184	152	48.7	1,7	1.2	Q
17441−2411	O	...	15.6	42.8	191.1	106.5	...	1	1.9	R
17534+2603	O	F2Ibe	5.5	97.5	54.5	13.4	6.04	1	1	...
18071−1727	O	...	...	23.1	76.6	83.5	...	1	...	F, M
18095+2704	O	F3Ib	10.4	45.1	125.7	27.8	5.6	1	1.9	Y
18184−1302[iv]	C	Be	13.9	336.0	597.5	253.2	436.0	1	1.7	...
18184−1623[v]	C	O+	8.4	70	325	117	584	5	1.2	T
18276−1431	O	K5-B9	...	22.7	132.0	120.0	38.6	1	...	F
19075+0921[i]	C	M	...	133.0	163.7	54.9	...	1	4	A,F
19192+0922[i]	O	M	...	127.2	155.0	41.4	9.8	1	1.3	E
19244+1115[iii]	O	F8Ia	8.5	1346.0	2314.0	717.7	185.8	1	3.4	E
19343+2926	O	B0.5IV	11.7	17.5	59.8	118.4	68.0	...	2.5	...
19374+2359	O	...	18.1	23.6	98.2	70.9	...	8	5.2	M,Z
19386+0155	...	F	11.2	17.4	47.4	18.6	3.8	...	5.3	M

TABLE 1—*Continued*

IRAS ID	C/O[a]	Sp. Type	V	F_{12} [Jy]	F_{25} [Jy]	F_{60} [Jy]	F_{100} [Jy]	Mid-IR Sp.[b]	D[kpc]	Ref.[c]
19454+2920	C	...	...	17.3	89.6	54.4	14.7	1	...	A,F
19477+2401	O	...	22.2	11.2	54.9	27.1	...	2	...	Z
19480+2504	C	...	...	20.8	67.9	43.2	...	1	...	A,F
20000+3239	C	G8Ia	13.2	15.0	71	30	...	2	...	F,U
20004+2955	O	G7Ia	8.9	31.7	37	4.7	...	1	...	S
20028+3910	...	...	17.8	41.8	210.8	143.1	46.5	1	...	F,Z
20043+2653	O	...	...	17.9	42	20.3	7.5	1	...	D
20077−0625	O	M	8.5	1255	1061	215.5	63.7	1	0.65	E
21537+6435	...	...	...	6.9	26.1	13.3	...	...	...	...
22036+5306[c]	O	...	...	8.4	46.3	107	50.7	1	...	C
22142+5206[d]	O	...	21.1	20.8	92.4	171.5	139.6	8	...	...
22223+4327	C	G0Ia	9.7	2.1	37.1	22.4	9.5	2	...	F,U
22480+6002	O	K0:Ia	10.4	141.9	175.2	39.8	...	1	...	...
22574+6609	C	...	24	9.0	29.5	20.6	7.2	...	...	X
23166+1655[i]	C	M	...	706.7	775.6	248.5	73.7	1	1.2	B
23304+6147	C	G2Ia	13.1	11.4	59.1	26.6	...	...	...	F,U
23321+6545	C/O	...	...	13.7	85.6	64	19.3	1	...	A,F,H

[a] C = carbon rich; O = oxygen rich; C/O = both carbon and oxygen rich

[b] References for Mid-IR spectra: 1. Olnon & Raimond (1986; *IRAS* LRS Atlas); 2. Kwok, Hrivnak & Geballe (1995); 3. Gillet & Soifer (1976); 4. Buss et al. (1990); 5. Volk & Cohen (1989); 6. Volk & Cohen (1990); 7. Justtanont et al. (1992); 8. Volk et al. (1991)

[c]References for other information: SIMBAD for *IRAS* measurements of all sources and for V and spectral type for many sources; Oudmaijer et al. (1992) for V and spectral type of many sources; Hrivnak (1998) for V and spectral type of many sources; A. Volk, Kwok & Woodsworth (1993); B. Groenewegen et al. (1998); C. Te Lintel Hekkert (1991); D. Manchado et al. (1989); E. Loup et al. (1993); F. Omont et al. (1993); G. Hu et al. (1993a); H. Likkel (1989); I. Cohen et al. (1975); J. Iyengar & Parthasarathy (1997); K. Hu et al. (1994); L. Mauron, Le Borgne & Picquette (1989); M. van der Veen, Habing & Geballe (1989); N. Silva et al. (1993); O. Hu et al. (1993b); P. Zijlstra et al. (1989); Q. Skinner et al. (1994); R. Kwok et al. (1996); S. Hrivnak, Kwok & Volk (1989); T. Robberto & Herbst (1998); U. Hrivnak (1995); V. Hrivnak & Kwok (1998); W. Hrivnak, Kwok, & Boreiko (1985); X. Hrivnak & Kwok (1991); Y. Hrivnak, Kwok & Volk (1988); Z. Hrivnak et al. (1999); AA. Waters et al. (1998)

[c]HD235718 (a.k.a. SAO 34043), a V=9.5 magnitude B9 star is NOT associated with this source. See text.

[d]This source is located 7″ north of *IRAS* coordinates. See text.

[i]extreme AGB star

[ii]very young planetary nebula

[iii]supergiant

[iv]probably pre-main sequence star

[v]luminous blue variable (LBV)

[vi]RV Tauri star

TABLE 2
MIRAC2 and Berkcam Observing Parameters

Identification	RA(2000)	DEC(2000)	Date, Tel[a], Cam[b]	λ ($\Delta\lambda$) [μm]	Standard
IRAS 00210+6221	00:23:51.1	+62:38:07	11/7/95, I, M	12.5 (10.0%)	βAnd
IRAS 00470+6429	00:50:07.2	+64:45:46	11/10/95, I, M	10.6 (8.1-13.1)	βAnd
IRAS 01144+6658	01:17:51.6	+67:13:52	11/10/95, I, M	8.8 (10.0%)	βAnd
(AFGL 190)			11/10/95, I, M	12.5 (10.0%)	βAnd
IRAS 01174+6110	01:20:44.3	+61:26:21	11/7/95, I, M	11.7 (10.0%)	βAnd
IRAS 01304+6211	01:33:51.2	+62:26:53	11/7/95, I, M	9.8 (10.0%)	βAnd
(OH 127.8+0.0)					
(V* V669 Cas)					
IRAS 02143+5852	02:17:57.9	+59:05:51	11/22/95, U, M	11.7 (10.0%)	βPeg
IRAS 02152+2822	02:18:06.6	+28:36:48	12/14/92, U, B	11.3CVF (10%)	βAnd
IRAS 02229+6208	02:26:41.8	+62:21:22	11/7/95, I, M	8.8 (10.0%)	βAnd
			11/7/95, I, M	9.8 (10.0%)	βAnd
			11/7/95, I, M	11.7 (10.0%)	βAnd
			11/7/95, I, M	12.5 (10.0%)	βAnd
			11/7/95, I, M	20.6 (7.0%)	αTau
HD 20041	03:15:48.0	+57:08:26.2	11/22/95,U, M	11.7 (10.0%)	βPeg
IRAS 04386+5722	04:42:48.3	+57:27:46.7	11/10/95, I, M	12.5 (10.0%)	αTau
IRAS 05089+0459	05:11:36.0	+05:03:26	11/22/95, U, M	11.7 (10.0%)	αTau
IRAS 05113+1347	05:14:07.8	+13:50:28	11/7/95, I, M	11.7 (10.0%)	αTau
IRAS 05341+0852	05:36:55.0	+08:54:09	11/7/95, I, M	8.8 (10.0%)	αTau
			11/7/95, I, M	11.7 (10.0%)	αTau
			11/23/95, U, M	11.7 (10.0%)	αTau
IRAS 06176−1036	06:19:58.2	−10:38:13.7	12/13/92, U, B	8.2CVF (10%)	αCMa
(Red Rectangle)			12/13/92, U, B	10.0CVF (10%)	αCMa
(HD 44179)			12/9/92, U, B	11.3CVF (10%)	αCMa
(AFGL 915)					
IRAS 06530−0213	06:55:30.5	−02:17:25	11/10/95, I, M	12.5 (10.0%)	αTau
IRAS 07239−3325	07:25:52.2	−33:31:22	11/23/95, U, M	10.6 (8.1-13.1)	αCMi
IRAS 07284−0940	07:30:47.4	−09:46:37	11/23/95, U, M	9.8 (10.0%)	αCMi
(HD 59693)					
(V* U Mon)					
IRAS 07331+0021	07:35:41.1	+00:14:59	11/23/95, U, M	8.8 (10.0%)	αCMa, αTau
(V* AI CMi)			11/23/95, U, M	20.6 (7.0%)	αCMi
IRAS 07399−1435	07:42:16.8	−14:42:52	11/6/95, I, M	8.8 (10.0%)	αCMa
(OH 231.8+4.2)			11/6/95, I, M	9.8 (10.0%)	αCMa
			11/6/95, I, M	11.7 (10.0%)	αCMa
			11/6/95, I, M	18.0 (10.0%)	αCMa
			11/6/95, I, M	20.6 (7.0%)	αCMa
IRAS 07430+1115	07:45:51.4	+11:08:16	11/23/95, U, M	8.8 (10.0%)	αTau
			11/7/95, I, M	11.7 (10.0%)	αTau
IRAS 08005−2356	08:02:41.9	−24:04:48	11/22/95, U, M	9.8 (10.0%)	αCMi, βPeg
IRAS 09032−3953	09:05:07.2	−40:05:11	11/22/95, U, M	8.8 (10.0%)	αCMi
IRAS 09371+1212	09:39:53.6	+11:58:54	11/23/95, U, M	3.8 (16.0%)	αCMa
(Frosty Leo)			11/23/95, U, M	10.6 (8.1-13.1)	αCMi

TABLE 2—*Continued*

Identification	RA(2000)	DEC(2000)	Date, Tel[a], Cam[b]	λ ($\Delta\lambda$) [μm]	Standard
IRAS 10131+3049	10:16:02.0	+30:34:19	6/9/92, U,B	11.5 (10%)	μUMa
(CIT 6)					
(IRC +30219)					
IRAS 10158−2844	10:18:07.6	−28:59:32	6/8/92, U, B	8.5CVF (10%)	αBoo, BS4104
(HR 4049)			6/7/92, U, B	9.7CVF (10%)	αBoo, BS4104
(HD 89353)					
IRAS 11472−0800	11:49:48.4	−08:17:21	11/24/95, U, M	9.8 (10.0%)	δVir, μUMa
IRAS 15465+2818	15:48:34.3	+28:09:25	5/15/91, I, B	12.5CVF (10%)	αBoo
(R CrB)					
IRAS 16342−3814	16:37:40.0	−38:20:14	6/3/95, I, M	9.8 (10.0%)	σLib
			6/3/95, I, M	12.5 (10.0%)	αBoo, σLib
			6/3/95, I, M	17.8 (2.6%)	ηSgr
			6/3/95, I, M	20.6 (7.0%)	σLib, ηSgr
IRAS 16559−2957	16:59:08.1	−30:01:41	6/3/95, I, M	12.5 (10.0%)	ηSgr
IRAS 17028−1004	17:05:37.9	−10:08:27	5/16/91, I, B	8.1CVF (1.3%)	αHer
(M 2−9)			5/16/91, I, B	8.5CVF (10%)	αHer
			5/16/91, I, B	9.7CVF (1.3%)	αHer
			5/16/91, I, B	12.6CVF (1.3%)	αHer
			5/16/91, I, B	12.8CVF (1.3%)	αHer
IRAS 17088−4221	17:12:21.5	−42:25:08	6/3/95, I, M	12.5 (10.0%)	ηSgr
IRAS 17106−3046	17:13:51.6	−30:49:42	6/7/95, I, M	18.0 (10.0%)	ηSgr
IRAS 17150−3224	17:18:20.0	−32:27:23	6/5/95, I, M	8.1CVF (1.8%)	ηSgr, αSco
			6/5/95, I, M	9.8 (10.0%)	αSco
			6/3/95, I, M	12.5 (10.0%)	ηSgr
IRAS 17245−3951	17:28:04.7	−39:53:44	6/3/95, I, M	12.5 (10.0%)	ηSgr
IRAS 17347−3139	17:38:00.6	−31:40:54	6/5/95, I, M	9.8 (10.0%)	ηSgr, αSco
			6/5/95, I, M	12.5 (10.0%)	ηSgr, αSco
			6/5/95, I, M	20.6 (7.0%)	ηSgr, αSco
IRAS 17436+5003	17:44:55.43	+50:02:39.9	6/7/95, I, M	18.0 (10.0%)	γDra
(HD 161796)			6/7/95, I, M	20.6 (7.0%)	γDra
(V* V814 Her)					
IRAS 17441−2411	17:47:13.0	−24:12:54	6/3/95, I, M	11.3CVF (1.8%)	ηSgr, αHer
			6/3/95, I, M	12.5 (10.0%)	ηSgr
IRAS 17534+2603	17:55:25.1	+26:03:00	5/15/91, I, B	12.5CVF (10%)	αHer
(89 Her)					
(HD 163506)					
IRAS 18071−1727	18:10:05.9	−17:26:35	6/6/95, I, M	9.8 (10.0%)	ηSgr
			6/6/95, I, M	12.5 (10.0%)	ηSgr
IRAS 18095+2704	18:11:30.6	+27:05:16	6/8/92, U, B	8.5CVF (10%)	αLyr
(OH 53.8+20.2)				11.0 (10%)	αLyr
IRAS 18184−1302	18:21:16	−13:01:27	6/9/92, U, B	8.2CVF (10%)	αLyr
(MWC 922)				12.2 (10%)	αLyr
IRAS 18184−1623	18:21:19.46	−16:22:26.0	6/4/95, I, M	8.8 (10.0%)	σLib
(HD 168625)			6/5/95, I, M	12.5 (10.0%)	ηSgr
(V* V4030 Sgr)			6/3/95, I, M	12.5 (10.0%)	βPeg
			6/4/95, I, M	20.6 (7.0%)	αHer

TABLE 2—*Continued*

Identification	RA(2000)	DEC(2000)	Date, Tel[a] Cam[b]	λ ($\Delta\lambda$) [μm]	Standard
IRAS 18276−1431	18:30:30.37	−14:28:53.2	6/6/95, I, M	9.8 (10.0%)	αLyr, αSct
(OH 17.7−2.0)			6/6/95, I, M	12.5 (10.0%)	αLyr, αSct
IRAS 19075+0921	19:09:57.1	+09:26:52	6/9/92, U, B	8.2CVF (10%)	αLyr
(AFGL 2333)			6/9/92, U, B	12.2CVF (10%)	αLyr
IRAS 19192+0922	19:21:36.5	+09:27:56	6/8/92, U, B	12.5CVF (10%)	γAql
(OH 44.8−2.3)					
IRAS 19244+1115	19:26:48.30	+11:21:08.7	6/4/95, I, M	9.8+20% (10.0%)	αAql
(IRC +10420)			6/4/95, I, M	20.6 (7.0%)	αHer
(V* V1302 Aql)					
IRAS 19343+2926	19:36:17.5	+29:32:50	5/16/91, I, B	8.5CVF (10%)	αHer
(M 1−92)					
IRAS 19374+2359	19:39:35.7	+24:06:23	6/5/95, I, M	9.8 (10.0%)	αLyr
			6/5/95, I, M	12.5 (10.0%)	αAql
			6/5/95, I, M	20.6 (7.0%)	αAql, αLyr
IRAS 19386+0155	19:41:08.2	+02:02:31	11/10/95, I, M	9.8 (10.0%)	γAql
IRAS 19454+2920	19:47:24.3	+29:28:16	6/6/95, I, M	9.8 (10.0%)	αLyr
IRAS 19477+2401	19:49:54.4	+24:08:51	6/7/95, I, M	9.8 (10.0%)	αLyr
			11/10/95, I, M	12.5 (10.0%)	γAql
IRAS 19480+2504	19:50:07.8	+25:12:00	6/6/95, I, M	9.8 (10.0%)	αLyr
IRAS 20000+3239	20:01:59.4	+32:47:32	6/3/95, I, M	8.1CVF (1.8%)	βPeg
			6/3/95, I, M	12.5 (10.0%)	βPeg
			6/6/95, I, M	12.5 (10.0%)	βPeg
IRAS 20004+2955	20:02:27.3	+30:04:25	6/7/95, I, M	9.8 (10.0%)	αLyr
(V* V1027 Cyg)					
IRAS 20028+3910	20:04:36.1	+39:18:44	11/10/95, I, M	9.8 (10.0%)	ϵCyg
			11/10/95, I, M	12.5 (10.0%)	ϵCyg
IRAS 20043+2653	20:06:22.9	+27:02:11	11/22/95, U, M	11.7 (10.0%)	βPeg
IRAS 20077−0625	20:10:27.4	−06:16:16	6/7/92, U, B	12.2CVF (10%)	γAql
(IRC −10529)					
IRAS 21537+6435	21:55:04	+64:49:52	11/10/95, I, M	12.5 (10.0%)	ϵCyg, SAO19687
IRAS 22036+5306	22:05:32.2	+53:22:10	11/23/95, U, M	8.8 (10.0%)	βPeg
			6/7/95, I, M	12.5 (10.0%)	βPeg
IRAS 22142+5206	22:16:10.3	+52:21:32	11/10/95, I, M	8.8 (10.0%)	βPeg
			11/10/95, I, M	12.5 (10.0%)	βPeg
IRAS 22223+4327	22:24:31	+43:43:09	6/7/95, I, M	12.5 (10.0%)	βPeg
			6/7/95, I, M	18.0 (10.0%)	βPeg
IRAS 22480+6002	22:49:59.1	+60:17:55	11/10/95, I, M	8.8 (10.0%)	βPeg, K star
			11/10/95, I, M	9.8 (10.0%)	βPeg, K star
			11/10/95, I, M	18.0 (10.0%)	βPeg, K star
IRAS 22574+6609	22:59:18.4	+66:25:48	11/10/95, I, M	8.8 (10.0%)	βPeg, K star
			6/7/95, I, M	12.5 (10.0%)	βPeg
IRAS 23166+1655	23:19:12.3	+17:11:35	6/2/92, U, B	8.5CVF (10%)	βPeg
(AFGL 3068)			12/13/92, U, B	8.5CVF (10%)	βPeg
			12/13/92, U, B	12.5CVF (10%)	βPeg
			12/13/92, U, B	11.3CVF (10%)	βPeg

TABLE 2—*Continued*

Identification	RA(2000)	DEC(2000)	Date, Tel[a], Cam[b]	λ ($\Delta\lambda$) [μm]	Standard
IRAS 23304+6147	23:32:44.5	+62:03:58	6/5/95, I, M	12.5 (10.0%)	βPeg, αLyr
			6/6/95, I, M	12.5 (10.0%)	βPeg
			6/6/95, I, M	20.6 (7.0%)	βPeg
IRAS 23321+6545	23:34:21.8	+66:01:53	11/7/95, I, M	12.5 (10.0%)	βAnd, βPeg
			11/10/95, I, M	12.5 (10.0%)	βPeg, SAO19687

[a]Telescope − I: IRTF, U: UKIRT

[b]Camera − M: MIRAC2, B: Berkcam

TABLE 3

OBSERVED FLUXES AND SIZES OF OBJECTS IN MIRAC2 AND BERKCAM MID-IR SURVEY

IRAS Identification	λ [μm]	F [Jy]	Source			PSF			Standard Star
			Size[a][″]	EL[b]	PA[c]	Size[a][″]	EL[b]	PA[c]	
00210+6221	12.5	33	1.10	0.10	72	1.10	0.06	97	βAnd
						1.14	0.04	62	βAnd
00470+6429	10.6	3	1.15	0.36	71	1.05	0.16	14	βAnd
01144+6658	8.8	157	0.97	0.18	76	0.90	0.03	89	βAnd
						0.86	0.04	43	βAnd
	12.5	260	1.25	0.14	77	1.11	0.03	80	βAnd
01174+6110	11.7	2	1.15	0.12	98	1.13	0.06	89	βAnd
						1.12	0.10	85	βAnd
01304+6211	9.8	73	1.06	0.08	88	1.10	0.13	82	βAnd
						1.14	0.02	26	βAnd
02143+5852	11.7	···	0.96	0.06	165	0.98	0.11	80	βPeg
02152+2822	11.3	162	1.00	0.15	174	1.20	0.09	163	βAnd
02229+6208	8.8	30	1.10	0.07	72	0.90	0.06	49	βAnd
						0.99	0.08	65	βAnd
	9.8	41	1.11	0.05	51	0.97	0.02	26	βAnd
						0.98	0.07	59	βAnd
	11.7	87	1.27	0.10	66	1.05	0.07	58	βAnd
						1.13	0.06	89	βAnd
	12.5	90	1.29	0.07	63	1.14	0.04	62	βAnd
						1.10	0.06	70	βAnd
	20.6	86	1.93	0.21	95	1.67	0.06	56	αTau
04386+5722	12.5	15	1.09	0.06	47	1.15	0.12	87	αTau
						1.18	0.12	83	αTau
05089+0459	11.7	···	1.08	0.17	90	0.96	0.15	90	αTau
05113+1347	11.7	4	1.12	0.05	38	1.07	0.06	51	αTau
05341+0852	8.8	1	1.06	0.24	31	1.00	0.10	114	αTau
						1.10	0.16	123	αTau
	(11/7) 11.7	4	0.99	0.16	47	1.07	0.06	51	αTau
	(11/23) 11.7	···	0.92	0.09	96	0.89	0.20	97	αTau
06176−1036	8.2	323	1.40	0.32	111	1.36	0.21	83	αCMa
	10.0	251	1.14	0.04	134	1.21	0.01	174	αCMa
	11.3	360	1.32	0.33	102	1.21	0.17	92	αCMa
06530−0213	12.5	12	1.18	0.06	47	1.15	0.12	87	αTau
07239−3325	10.6	···	0.74	0.09	98	0.98	0.26	89	αCMi
07284−0940	9.8	···	1.05	0.30	88	1.01	0.31	88	αCMi
07331+0021	8.8	···	0.97	0.25	89	0.89	0.20	97	αTau
						1.01	0.24	85	αCMa
	20.6	···	1.46	0.14	92	1.37	0.08	79	αCMi
07399−1435	8.8	25	1.66	0.25	43	1.15	0.14	21	αCMa
	9.8	20	1.96	0.20	22	0.98	0.11	116	αCMa
	11.7	30	1.61	0.25	26	1.05	0.04	20	αCMa
	18.0	204	2.10	0.25	13	1.30	0.04	20	αCMa
	20.6	290	2.28	0.19	9	1.75	0.27	0	αCMa
07430+1115	8.8	···	0.93	0.18	96	0.89	0.20	97	αTau
	11.7	6	1.10	0.21	39	1.07	0.23	50	αTau
08005−2356	9.8	···	0.96	0.17	95	0.98	0.25	90	αCMi
						1.07	0.19	103	βPeg
09032−3953	8.8	···	1.00	0.18	107	0.89	0.13	90	αCMi

TABLE 3—*Continued*

IRAS Identification	λ [μm]	F [Jy]	Source			PSF			Standard Star
			Size[a][″]	EL[b]	PA[c]	Size[a][″]	EL[b]	PA[c]	
09371+1212	3.8	···	1.07	0.08	144	1.29	0.06	93	αCMa
	10.6	···	1.03	0.33	81	0.98	0.26	89	αCMi
10131+3049	11.5	2672	1.01	0.06	121	1.06	0.05	29	μUMa
10158−2844	8.5	52	1.52	0.04	127	1.78	0.20	176	αBoo
						1.52	0.06	170	BS4104
	9.7	30	1.58	0.04	29	1.46	0.11	114	αBoo
						1.24	0.23	176	BS4104
11472−0800	9.8	···	1.34	0.25	81	1.45	0.33	94	δVir
						1.03	0.15	103	μUMa
15465+2818	12.5	24	1.21	0.05	81	1.15	0.32	99	αBoo
16342−3814	9.8	7	1.67	0.23	66	0.85	0.02	66	σLib
						0.87	0.04	15	σLib
	12.5	14	1.43	0.23	60	1.00	0.06	76	αBoo
						1.04	0.07	15	σLib
	17.8	127	1.76	0.24	64	1.30	0.01	100	ηSgr
						1.34	0.07	171	ηSgr
	20.6	200	1.87	0.15	59	1.55	0.04	32	σLib
						1.61	0.02	86	ηSgr
16559−2957	12.5	11	1.02	0.04	34	1.01	0.01	69	ηSgr
						1.03	0.05	42	ηSgr
17028−1004	8.1	30	1.00	0.21	111	0.90	0.25	83	αHer
	8.5	41	0.89	0.22	105	0.92	0.12	75	αBoo
						0.88	0.30	88	αHer
	9.7	29	1.21	0.22	138	0.97	0.26	88	αHer
	12.6	44	1.31	0.17	166	1.20	0.06	126	αHer
	12.8	43	1.49	0.16	142	1.18	0.12	119	αHer
						1.22	0.21	127	αHer
17088−4221	12.5	62	1.10	0.11	13	1.04	0.04	104	ηSgr
						1.01	0.01	69	ηSgr
17106−3046	18.0	36	1.46	0.05	88	1.37	0.02	61	ηSgr
						1.35	0.03	43	ηSgr
17150−3224	8.1	15	1.22	0.13	68	0.87	0.04	96	ηSgr
						1.06	0.13	70	αSco
	9.8	24	1.26	0.11	121	0.98	0.05	172	αSco
						0.97	0.07	172	αSco
	12.5	74	1.27	0.11	72	1.03	0.05	42	ηSgr
						1.16	0.10	62	ηSgr
17245−3951	12.5	3	1.15	0.09	34	1.03	0.05	42	ηSgr
						1.16	0.10	62	ηSgr
17347−3139	9.8	8	1.33	0.20	138	0.96	0.04	165	αSco
						0.96	0.04	158	αSco
	12.5	28	1.20	0.13	145	1.05	0.03	125	αSco
						1.00	0.02	173	αSco
	20.6	102	1.62	0.04	136	1.61	0.01	90	αSco
						1.55	0.01	94	ηSgr
17436+5003	18.0	113	2.78	0.08	75	1.47	0.11	80	γDra
	20.6	195	2.77	0.08	74	1.71	0.11	62	γDra

TABLE 3—*Continued*

IRAS Identification	λ [μm]	F [Jy]	Source			PSF			Standard Star
			Size[a]["]	EL[b]	PA[c]	Size[a]["]	EL[b]	PA[c]	
17441−2411	11.3	37	1.57	0.15	64	1.33	0.10	70	αHer
						1.29	0.10	82	ηSgr
	12.5	51	1.46	0.13	58	1.16	0.09	52	ηSgr
						1.27	0.06	86	ηSgr
17534+2603	12.5	53	1.24	0.09	80	1.07	0.11	107	αHer
18071−1727	9.8	7	0.99	0.08	67	0.84	0.06	31	ηSgr
						0.88	0.06	39	ηSgr
	12.5	36	1.06	0.07	52	1.08	0.09	35	ηSgr
18095+2704	8.5	12	1.00	0.01	45	1.03	0.11	159	αLyr
	11.0	45	0.94	0.02	111	1.13	0.13	132	αLyr
18184−1302	8.2	171	1.27	0.07	119	1.34	0.23	104	ηSgr
						0.90	0.13	136	αLyr
	12.2	305	1.27	0.05	30	1.02	0.23	170	αLyr
18184−1623[d]	8.8	41	18.4	0.39	22	1.83	0.29	148	σLib
						1.82	0.24	39	σLib
	(6/3) 12.5	64	18.2	0.26	36	1.00	0.05	85	βPeg
						0.99	0.02	44	βPeg
	(6/5) 12.5	59	17.9	0.32	22	1.95	0.53	150	ηSgr
	20.6	302	20.5	0.43	23	1.80	0.03	111	αHer
18276−1431	9.8	13	1.13	0.12	34	0.94	0.15	48	αLyr
						0.91	0.02	75	αSct[e]
	12.5	27	1.19	0.08	62	1.06	0.05	51	αLyr
						1.13	0.13	82	αSct[e]
19075+0921	8.2	75	1.04	0.11	171	0.90	0.13	136	αLyr
	12.2	149	1.03	0.08	6	1.02	0.23	170	αLyr
19192+0922	12.5	229	1.13	0.08	131	1.05	0.06	108	γAql
19244+1115	9.8	1987	1.31	0.16	45	1.18	0.09	58	αAql
	20.6	3128	2.31	0.15	63	1.80	0.03	111	αHer
19343+2926	8.5	16	1.04	0.16	100	0.88	0.30	88	αHer
19374+2359	9.8	18	1.21	0.05	5	0.91	0.04	55	αLyr
	12.5	28	1.27	0.07	17	1.05	0.11	63	αAql
	20.6	176	1.83	0.05	57	1.57	0.02	116	αLyr
						1.58	0.14	113	αAql
19386+0155	9.8	10	1.19	0.20	86	1.20	0.24	87	γAql
19454+2920	9.8	14	0.97	0.07	24	0.94	0.15	48	αLyr
						0.92	0.09	89	αLyr
19477+2401	9.8	6	0.97	0.08	74	1.00	0.13	71	αLyr
						1.00	0.13	77	αLyr
	12.5	13	1.35	0.17	88	1.33	0.17	90	γAql
19480+2504	9.8	14	0.95	0.04	44	0.94	0.15	48	αLyr
						0.92	0.09	89	αLyr
20000+3239	8.1	5	1.13	0.21	85	1.01	0.08	70	βPeg
	(6/3) 12.5	14	1.27	0.11	80	1.00	0.05	85	βPeg
						0.99	0.02	44	βPeg
	(6/6) 12.5	14	1.14	0.05	55	1.03	0.11	4	βPeg
						1.00	0.06	11	βPeg
20004+2955	9.8	54	0.93	0.06	80	0.96	0.10	68	αLyr
						1.00	0.13	71	αLyr

TABLE 3—*Continued*

IRAS Identification	λ [μm]	F [Jy]	Source			PSF			Standard Star
			Size[a]["]	EL[b]	PA[c]	Size[a]["]	EL[b]	PA[c]	
20028+3910	9.8	23	1.22	0.19	100	1.08	0.18	89	ϵCyg
	12.5	51	1.42	0.21	92	1.32	0.18	91	ϵCyg
						1.32	0.17	97	ϵCyg
20043+2653	11.7	···	1.05	0.08	30	1.00	0.12	103	βPeg
						0.98	0.11	80	βPeg
20077−0625	12.2	1089	1.13	0.03	172	1.27	0.09	162	γAql
21537+6435	12.5	9	1.16	0.14	72	1.32	0.18	91	ϵCyg
						1.32	0.17	97	ϵCyg
						1.35	0.16	85	SAO19687[e]
22036+5306	12.5	6	1.20	0.14	72	1.33	0.33	88	βPeg
						1.04	0.05	87	βPeg
22142+5206	8.8	7	1.04	0.13	97	1.08	0.21	92	βPeg
						0.90	0.10	75	βPeg
	12.5	24	1.42	0.22	94	1.26	0.16	90	βPeg
22223+4327	12.5	2	1.83	0.10	89	1.09	0.18	88	βPeg
						1.01	0.06	86	βPeg
	18.0	9	1.71	0.09	140	1.31	0.01	105	βPeg
						1.33	0.03	78	βPeg
22480+6002	8.8	91	0.99	0.15	80	0.90	0.10	75	βPeg
						0.93	0.24	83	K star[e]
	9.8	195	1.10	0.16	73	0.89	0.04	19	βPeg
						0.97	0.11	76	K star[e]
	18.0	184	1.76	0.15	88	1.49	0.05	110	βPeg
						1.64	0.13	84	βPeg
22574+6609	8.8	5	1.12	0.26	87	1.08	0.21	92	βPeg
						0.90	0.10	75	βPeg
						1.26	0.34	88	K star[e]
	12.5	9	1.21	0.15	89	1.04	0.05	87	βPeg
						1.08	0.12	92	βPeg
23166+1655	(6/2) 8.5	557	1.04	0.07	178	1.08	0.13	120	βPeg
	(12/13) 8.5	284	1.09	0.12	129	0.81	0.08	132	βPeg
	11.3	394	1.00	0.11	141	0.93	0.12	149	βPeg
	12.5	435	1.12	0.07	108	1.18	0.06	125	βPeg
23304+6147	(6/5) 12.5	13	1.45	0.23	83	1.10	0.08	80	αLyr
						1.01	0.05	25	βPeg
	(6/6) 12.5	12	1.37	0.16	82	1.00	0.06	11	βPeg
						1.02	0.08	18	βPeg
	20.6	58	1.62	0.03	42	1.56	0.04	31	βPeg
23321+6545	(11/7) 12.5	15	1.18	0.06	90	1.10	0.06	97	βAnd
						1.14	0.04	62	βAnd
	(11/10) 12.5	18	1.15	0.10	87	1.26	0.16	90	βPeg
						1.11	0.03	80	βAnd
						1.35	0.16	85	SAO19687[e]

[a]The major axis of the 50% contour level.
[b]EL $= 1 - b/a$, a and b being major and minor axis lengths.
[c]Measured counter-clockwise from north in degrees.
[d]F, Size, EL, and PA refer to those of the entire shell structure.
[e]Not a flux calibrator.

TABLE 4A

RESOLVED SOURCES AND THEIR MORPHOLOGY

IRAS ID	λ [μm]	Size[a]["]	PA	Mid−IR Morph. Class	C/O[b]	Type[c]	Optical Morph. Class	Ref.[d]
02229+6208	8.8	1.1	...	unknown[d]	C	PPN	star+bipolar	7
	9.8	1.1	...					
	11.7	1.3	...					
	12.5	1.3	...					
	20.6	1.9	...					
06176−1036	8.2	2.7×1.7	16	core/elliptical	C/O	PPN	bipolar	1
(Red Rectangle)	10.0	2×1.6	98					
	11.3	2.6×1.7	18					
07399−1435	8.8	2.8×2.2	41	core/elliptical	O	Extreme AGB	bipolar	2
(OH 231.8+4.2)	9.8	3.4×2.9	22					
	11.7	2.9×2.4	29					
	18.0	3.6×2.9	17					
	20.6	3.8×3.2	11					
16342−3814	9.8	2.7×2.1	68	core/elliptical	O	Extreme AGB	bipolar	7
	12.5	2.4×1.8	63					
	17.8	2.7×2.1	60					
	20.6	2.9×2.4	67					
17028−1004	8.1	1.8×1.3	97	core/elliptical	O	Young PN	bipolar	3
(M 2−9)	8.5	1.6×1.1	101					
	9.7	2×1.3	133					
	12.6	2.5×2.2	114					
	12.8	2.7×2.2	146					
17150−3224	8.1	2.1×1.7	56	core/elliptical	O	PPN	bipolar	4,5,6,7
	9.8	2.1×1.8	106					
	12.5	2.0×1.8	79					
17347−3139	9.8	2.1×1.8	136	core/elliptical	O	Young PN	unknown	...
	12.5	1.8×1.6	149					
	20.6	1.6×1.2	150					
17436+5003	18.0	2.8×2.3	99	toroidal	O	PPN	star+bipolar	7
(HD 161796)	20.6	2.8×2.1	95					
17441−2411	11.3	1.6	...	unknown[d]	O	PPN	bipolar	5,7
	12.5	1.5	...					
18184−1302	8.2	1.3	...	unknown[d]	?	Pre-MS	unknown	...
(MWC 922)	12.2	1.3	...					
18184−1623	8.8	18.4×11.2	22	toroidal	C	LBV/PPN	star+torus	8
(HD 168625)	12.5	18.2×13.5	36					
	20.6	20.5×11.7	23					
18276−1431	9.8	1.1	...	unknown[d]	O	PPN	unknown	...
(OH 17.7−2.3)	12.5	1.2	...					
19244+1115	9.8	1.3×1.2	58	core/elliptical	O	SG	bipolar	9
(IRC +10420)	20.6	2.3×1.9	75					
19374+2359	9.8	1.2×1.1	34	core/elliptical	O	PPN	star+round	10
	12.5	1.3×1.2	50					
	20.6	1.8×1.7	51					
20000+3239	8.1	1.1	...	unknown[d]	C	PPN	star+round	10
	12.5	1.1	...					

TABLE 4A—*Continued*

IRAS ID	λ [μm]	Size[a][″]	PA	Mid−IR Morph. Class	C/O[b]	Type[c]	Optical Morph. Class	Ref.[d]
22223+4327	12.5	1.9×1.7	108	toroidal	C	PPN	unknown	. . .
	18.0	1.9×1.8	152					
23304+6147	12.5	1.5	. . .	unknown[d]	C	PPN	star+round	10
	20.6	1.6	. . .					

[a]For extended sources, the size is major×minor axes of the 20% contour level. For marginally resolved sources (i.e. morph. class unknown), the size is the major axis of the 50% contour level which is, of course, an upper limit to the actual size of the source.

[b] C = carbon rich; O = oxygen rich; C/O = both carbon and oxygen rich

[c] PPN: Proto-Planetary Nebulae, PN: Planetary Nebulae, AGB: Asymptotic Giant Branch star, LBV: luminous blue variable, SG: Super Giant, and MS: Main Sequence

[d]1. Cohen et al. (1975); 2. Kastner et al. (1992); 3. Trammell, Goodrich, & Dinerstein (1995); 4. Hu et al. (1993b); 5. Kwok et al. (1996); 6. Kwok, Su & Hrivnak (1998); 7. Ueta, Meixner & Bobrowsky (1998); 8. Hutsemekers et al. (1994); 9. Humphreys et al. (1993); 10. Hrivnak et al. (1999)

[d] "Unknown" is assigned to sources which are only marginally resolved.

TABLE 4B

MID–INFRARED IMAGES FROM THE LITERATURE

IRAS/IR ID	alternate name	Mid-IR Morph. Class	Ref.[a]	C/O[b]	Type[c]	Optical Morph. Class	Ref.[d]
04296+3429	. . .	unresolved	2	C	PPN	star+multipolar	c
04395+3601	AFGL 618	core/elliptical	6	C	Young PN	bipolar	a
06176−1036	AFGL 915	core/elliptical	6	C/O	PPN	bipolar	b
07134+1005	HD56126	toroidal	2,3	C	PPN	star+bipolar	c
17436+5003	HD 161796	toroidal	7	O	PPN	star+bipolar	c
19114+0002	HD179821,AFGL 2343	toroidal	1	O	PPN/SG	star+multipolar	c
19500-1709	HD187885	unknown	2	C	PPN	unknown	. . .
AFGL 2688	Egg Nebula	core/elliptical	5,6	C	PPN	bipolar	d
21282+5050	. . .	toroidal	2,4	C	Young PN	star+bipolar	e
22272+5435	HD235858	toroidal	2,3	C	PPN	star+multipolar	c

[a] 1. Hawkins et al. (1995); 2. Meixner et al. (1997); 3. Dayal et al. (1998); 4. Meixner et al. (1993b); 5. Skinner et al. (1997); 6. Hora et al. (1996); 7. Skinner et al. (1994)

[b] C = carbon rich; O = oxygen rich; C/O = both carbon and oxygen rich

[c] PPN: Proto-Planetary Nebulae; PN: Planetary Nebulae

[d] a. Westbrook et al. (1975); b. Cohen et al. (1975); c. Ueta, Meixner, Bobrowsky (1998); d. Ney et al. (1975); e. Meixner (1993)